Revealing the Sub-Barrier Phase using a Spatiotemporal Interferometer with Orthogonal Two-Color Laser Fields of Comparable Intensity

Meng Han,[1] Peipei Ge,[1] Yun Shao,[1] Ming-Ming Liu,[1] Yongkai Deng,[1,2] Chengyin Wu,[1,2]
Qihuang Gong,[1,2] and Yunquan Liu[1,2,*]
[1]*Department of Physics and State Key Laboratory for Mesoscopic Physics, Peking University, Beijing 100871, China*
[2]*Collaborative Innovation Center of Quantum Matter, Beijing 100871, China*

(Received 28 April 2017; revised manuscript received 13 June 2017; published 14 August 2017)

We measure photoelectron momentum distributions of Ar atoms in orthogonally polarized two-color laser fields with comparable intensities. The synthesized laser field is used to manipulate the oscillating tunneling barrier and the subsequent motion of electrons onto two spatial dimensions. The subcycle structures associated with the temporal double-slit interference are spatially separated and enhanced. We use such a spatiotemporal interferometer to reveal sub-barrier phase of strong-field tunneling ionization. This study shows that the tunneling process transfers the initial phase onto momentum distribution. Our work has the implication that the sub-barrier phase plays an indispensable role in photoelectron interference processes.

DOI: 10.1103/PhysRevLett.119.073201

The phase of microscopic particles is a key ingredient to interpret their wavelike property. In the strong-field community, tunneling ionization is the footstone of numerous phenomena [1]. Electron tunneling through the suppressed Coulomb potential and traveling in continuum leave fingerprints not only on the amplitude of the electron wave packet (WP), but also on its phase distribution. Previous experiments mainly focused on the ionization amplitude or photoelectron momentum distributions; the phase of the tunneling wave packet is less studied. Especially for the accumulated phase when electron tunneling through the Coulomb barrier, i.e., the sub-barrier phase, it has a nonignorable contribution on the interference pattern of electron momentum distribution and is hard to be observed. Most classical or semiclassical models [2–5] have ignored the initial phase. However, "quantum" theories [6–8] pointed out that the action of an electron penetrating a laser-induced potential barrier is a complex number, where its real part is associated with the sub-barrier phase [9]. The crucial question is how it can be revealed through a reliable experimental scheme.

The intracycle interference with few-cycle pulses has been demonstrated [10], which results from the temporal double-slit interference between two WPs released in consecutive laser half-cycles. The temporal interferometer has been used to resolve electron sublaser-cycle dynamics [11]. The orthogonally polarized two-color (OTC) laser fields $(1\omega + 2\omega)$ can manipulate the ultrafast electron emission and its subsequent motion in both time and space [12–17]. For example, with a weak second harmonic in an OTC field, the intracycle interference fringes (two WPs released in one fundamental-field cycle) can be switched on or off [18]. However, the initial phase difference between those two WPs is tiny, and a weak second harmonic streaking field is insufficient to reveal its subtle effect. Strong Coulomb focusing also erases the effect. If one increases the intensity of the streaking field, e.g., in comparable-intensity OTC fields, the Coulomb focusing is reduced by the strong transverse field. And it emits four space-dependent WPs successively in one fundamental-field cycle, inducing more rich subcycle interference patterns [19]. The effect of the sub-barrier phase on the interferograms can be amplified with this scheme.

In this Letter, we present high-resolution photoelectron momentum distributions of Ar atoms in OTC fields with comparable intensities. Using this scheme, we introduce a spatiotemporal interferometer to reveal the sub-barrier phase of tunneling ionization. In the laser fields, the suppressed Coulomb barrier is spatially manipulated onto two spatial dimensions, and the successively released WPs carry different sub-barrier phases. The transverse intense second harmonic field arranges the interference among those WPs to achieve high-contrast spatially separated fringes. By comparison with simulations of the strong-field approximation (SFA) model [20–22], the Coulomb-corrected SFA (CCSFA) model [6,7], and the numerical solution of the time-dependent Schrödinger equation (TDSE), the signature of the sub-barrier phase on the final momentum distribution is identified.

Experimentally, the OTC pulse $\boldsymbol{E}(t) = E_{800}\cos(\omega_1 t)\boldsymbol{x} + E_{400}\cos(\omega_2 t + \Delta\varphi)\boldsymbol{z}$ was used, where E_{800} and E_{400} are electric-field amplitudes of the fundamental and the second-harmonic lights, respectively, and $\Delta\varphi$ is the phase delay between the two colors. The fundamental-field light was produced from a Ti:sapphire multipass amplifier (800 nm, 25 fs, 3 kHz), and the second-harmonic pulse was generated through frequency doubling with a 250-μm-thick β-barium borate crystal. The phase delay was controlled by using a pair of fused silica wedges with a precision of roughly 5 as ($\sim 0.004\pi$). We calibrated the phase delay by comparing the measured electron momentum distribution with the solution of TDSE. We measured the photoelectron momentum distributions of Argon atoms using cold-target recoil-ion reaction momentum spectroscopy [23].

In [24], the electron momentum distribution of strong-field ionization of atoms with the comparable-intensity OTC fields has been measured. However, the momentum resolution is not enough to reveal the clear interferograms. Here, we measured high-resolution electron momentum distributions with the comparable-intensity OTC fields to identify the sub-barrier effect. In Fig. 1, we illustrate the measured electron momentum distributions of Ar atoms in the polarization plane at the phase delay of $\Delta\varphi = 0$, 0.25π, 0.5π, 0.75π, respectively. The peak intensity of the fundamental light was $I_{800} = (0.72 \pm 0.05) \times 10^{14}\ \mathrm{W/cm^2}$ and that of the second harmonic was $I_{400} = (0.87 \pm 0.03) \times 10^{14}\ \mathrm{W/cm^2}$, which were calibrated according to the location of above-threshold ionization (ATI) peaks in the energy spectrum when only exposing the corresponding one-color light.

The electron momentum distributions are sensitive to the phase delay between the two fields. For $\Delta\varphi = 0$, although the synthesized laser vector potential is symmetrical with respect to the x axis (polarization direction of 800 nm light), the momentum distribution is not symmetrical with the p_x axis because of Coulomb scattering [24,25]. Within the SFA model, the electron momentum distributions at $\Delta\varphi = 0.25\pi$ and $\Delta\varphi = 0.75\pi$ are expected to be identical. However, because of the Coulomb scattering, the experimental distributions show very different patterns. Compared with the previous experiment [24], the measured electron momentum distributions reveal rich interference patterns at each phase delay. The observed concentric rings are associated with the intercycle interference and the radial fringes are generally related to the subcycle interference of multiple tunneling wave packets. The subcycle interference becomes the dominant contribution to the upper-half plane of momentum distribution at $\Delta\varphi = 0.5\pi$, appearing in a bouquetlike pattern. The high-resolution experimental data allow us to investigate the subcycle interference and resolve the fingerprint of the sub-barrier phase on the momentum distribution by comparison with theoretical simulation.

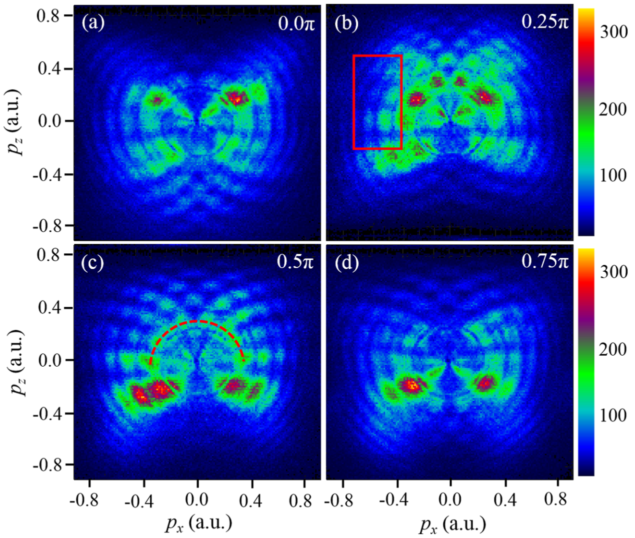

FIG. 1. Experimental electron momentum distributions of Argon in an OTC field in the polarization plane for $\Delta\varphi = 0$ (a), 0.25π (b), 0.5π (c), and 0.75π (d). The peak intensity of the fundamental light was $I_{800} = (0.72 \pm 0.05) \times 10^{14}\ \mathrm{W/cm^2}$ and that of the second harmonic was $I_{400} = (0.87 \pm 0.03) \times 10^{14}\ \mathrm{W/cm^2}$. The 800 and 400 nm fields are along the x and z axes, respectively. The data are integrated over an angular range $\theta = 90° \pm 30°$ where $\theta = \mathrm{acos}(p_y/\sqrt{p_y^2 + p_x^2 + p_z^2})$ is the angle between the electron momentum vector and the normal to the (p_x, p_z) plane.

Within the SFA, the transition matrix element is given by [26]

$$M_{\boldsymbol{p}}^{(\mathrm{SFA})} = -i \int_0^{t_f} d\tau \langle \boldsymbol{p} + \boldsymbol{A}(\tau) | \boldsymbol{r} \cdot \boldsymbol{E}(\tau) | \psi_0(\boldsymbol{r}) \rangle \times \exp\left(\int_0^{\tau} \frac{1}{2}[\boldsymbol{p} + \boldsymbol{A}(t')]^2 + I_p dt' \right), \qquad (1)$$

where $\boldsymbol{p}$ is the photoelectron canonical momentum, $\boldsymbol{A}(t)$ is the laser vector potential, t_f is the pulse turn-off time, $\psi_0(\boldsymbol{r})$ is the atomic initial-state wave function, and I_p is the ionization potential. The transition amplitude can be given by $M_{\boldsymbol{p}}^{(\mathrm{SFA})} = \sum_{i=1}^{4} f_{\psi_0}(\boldsymbol{p}, t_s^{(i)}, t_f) e^{iS_0(\boldsymbol{p}, t_s^{(i)}, t_f)}$, where $t_s^{(i)}$ is the saddle point governed by the equation $\frac{1}{2}[\boldsymbol{p} + \boldsymbol{A}(t_s^{(i)})]^2 + I_p = 0$. The preexponential factor $f_{\psi_0}(\boldsymbol{p}, t_s^{(i)}, t_f)$ is proportional to the matrix element $\langle \boldsymbol{p} + \boldsymbol{A}(\tau) | \boldsymbol{r} \cdot \boldsymbol{E} | \psi_0(\boldsymbol{r}) \rangle$, which does not affect the structure of interference patterns. The action of each WP $S_0(\boldsymbol{p}, t_s^{(i)}, t_f) = -\int_{t_s^{(i)}}^{t_f} \frac{1}{2}[\boldsymbol{p} + \boldsymbol{A}(t)]^2 + I_p dt$ plays the role on the interference. In the Coulomb-correction SFA model, the tunneling electron acquires a small extra action of $\Delta S_{cc} = -\int_{t_s^{(i)}}^{t_f} V[\boldsymbol{r}(t)] dt$, where $V[\boldsymbol{r}(t)]$ is the atomic potential with respect to the laser-induced trajectory $\boldsymbol{r}(t) = \boldsymbol{p}(t - t_s^{(i)}) + \int_{t_s^{(i)}}^{t} \boldsymbol{A}(t') dt'$. When the electron propagates under the barrier, the total complex-valued action $S_0 + \Delta S_{cc}$ of each trajectory is evaluated along the vertical path from the saddle point $t_s^{(i)}(\boldsymbol{p})$ to its real part $t_r^{(i)}(\boldsymbol{p})$. The imaginary part of the total action is related to the tunneling probability, given by $\Gamma \approx e^{-2\mathrm{Im}S_0} e^{-2\mathrm{Im}\Delta S_{cc}}$ [27]. The real part of the total action $\Phi_{\mathrm{sub}} = \mathrm{Re}[S_0(\boldsymbol{p}, t_s^{(i)}, t_r^{(i)})] + \mathrm{Re}[\Delta S_{cc}(\boldsymbol{p}, t_s^{(i)}, t_r^{(i)})]$ is the accumulated sub-barrier phase when tunneling through the potential. After the electron tunnels from the barrier,

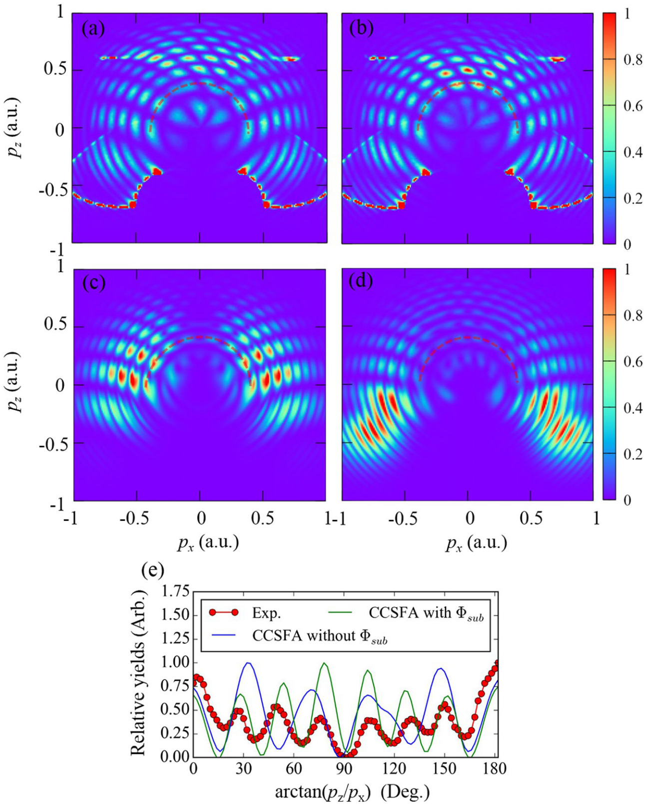

FIG. 2. Simulated electron momentum distributions at $\Delta\varphi = 0.5\pi$ are calculated by the CCSFA model without the sub-barrier phase (a), with the sub-barrier phase (b), the SFA model with numerical method (c), and the TDSE method (d). (e) The projection of the ionization probability along the dashed curves [$p_r = \sqrt{p_x^2 + p_z^2} = (0.35 \pm 0.01)$a.u.] with respect to the emission angle.

the electron motion is governed by Newton equation $\ddot{\boldsymbol{r}} = -\boldsymbol{r}/r^3 - \boldsymbol{E}(t)$ as well as the phase equation $\Phi_{\mathrm{prop}} = -\int_{t_r}^{t_f} \frac{1}{2}[\boldsymbol{p} + \boldsymbol{A}(t)]^2 + I_p + V[\boldsymbol{r}(t)]dt$ until the laser turns off. Finally, the asymptotic momenta on the detector are calculated by Kepler's laws after the laser pulse turns off.

We present the calculated electron momentum distributions by the CCSFA model with and without the sub-barrier phase at $\Delta\varphi = 0.5\pi$ in Figs. 2(a) and 2(b), respectively. The sub-barrier phase obviously affects the interval of the radial interference fringes, and especially increases the number of these fringes in the low-energy electron momentum distribution. The result by the CCSFA model with the sub-barrier phase agrees better with the measurement [Fig. 1(c)]. In Fig. 2(c), we show the result of the SFA model by solving Eq. (1) numerically, in which we choose the $3p$ state as the initial state $\psi_0(\boldsymbol{r})$ to match the Argon atom. The SFA model naturally includes the plain sub-barrier phase $\mathrm{Re}[S_0(\boldsymbol{p}, t_s, t_r)]$, but it has no effect on the Coulomb interaction in both sub-barrier and outside-barrier regions. In Fig. 2(d), we show the electron momentum distribution calculated by a TDSE solver [28] within the single-electron approximation. In the simulation, the $3p$ state in an effective potential $V_{\mathrm{eff}} = -[Z + (Z_{\mathrm{full}} - Z)e^{-r/r_s}]/r$ is used as the initial state, where $Z = 1$ and $Z_{\mathrm{full}} = 18$ are the asymptotic ion charges as $r \to \infty$ and $r \to 0$, respectively, and a screening length $r_s = 0.21494$ is tuned to match $I_p = 0.579$ a.u. for Argon. The laser field is synthesized by an eight-cycle $\sin^2$-envelope laser pulse at 800 nm, and the peaks of 800 and 400 nm electric fields are 0.045 and 0.05 a.u., respectively. The laser parameters are identical in all simulation in this work.

Along the dashed curve located at the first ATI ring in Fig. 2(a), there are six maxima in the CCSFA simulation without the sub-barrier phase, which does not agree with that of the measurement [Fig. 1(c)] and the TDSE result [Fig. 2(d)] (both show eight maxima). If the CCSFA simulation includes the sub-barrier phase [Fig. 2(b)], the better agreement is achieved. Because the standard SFA model naturally includes the plain sub-barrier phase $\mathrm{Re}[S_0(\boldsymbol{p}, t_s, t_r)]$, the calculated momentum distribution [Fig. 2(c)] also reveals the eight maxima in the same momentum area, which indicates that $\mathrm{Re}[S_0(\boldsymbol{p}, t_s, t_r)]$ plays a dominant role. In Fig. 2(e), we plot the projection of the experimental and simulated electron momentum distributions along the dashed curve. The simulation with the sub-barrier phase agrees with the experiment.

Apart from the number of maxima along the first ATI ring, below the red dashed curve there are both seven wings in the experimental and TDSE results. The calculated electron momentum distribution with the sub-barrier phase is more comparable with the experimental result and the *ab initio* solution of TDSE. Through comparison of the momentum distributions, one can find that the bouquetlike radial fringes related to the subcycle interference are sensitive to the sub-barrier phase.

To illustrate how to reveal the sub-barrier phase on the interferogram, we analyze the subcycle dynamics of tunneling electrons at $\Delta\varphi = 0.5\pi$. Figure 3(a) shows the synthesized electric field, the negative vector potentials of the 800 nm light and 400 nm light in one 800 nm cycle. As shown, the synthesized electric field has four temporal equal-amplitude peaks in one cycle, and it induces four WPs with equal amplitude but different sub-barrier phases. The spatial distributions of the four WPs in the polarization plane are also illustrated schematically. In Fig. 3(b), we illustrate the track of the end point of the synthesized electric-field vector in one 800 nm cycle. The four corner panels in Fig. 3(b) depict the instantaneous component laser fields at the tunnel moment. After tunneling, those four WPs are spatially driven to different directions (indicated by the green arrows) by the laser fields. If the WPs arrive at the same space, the interference occurs. Thus, the interaction geometry can be viewed as a spatiotemporal interferometer. At $\Delta\varphi = 0.5\pi$, WP1 and WP2 are driven into the right hemisphere of momentum plane, whereas WP3 and WP4 are driven into the left part, as seen in Fig. 3(c).

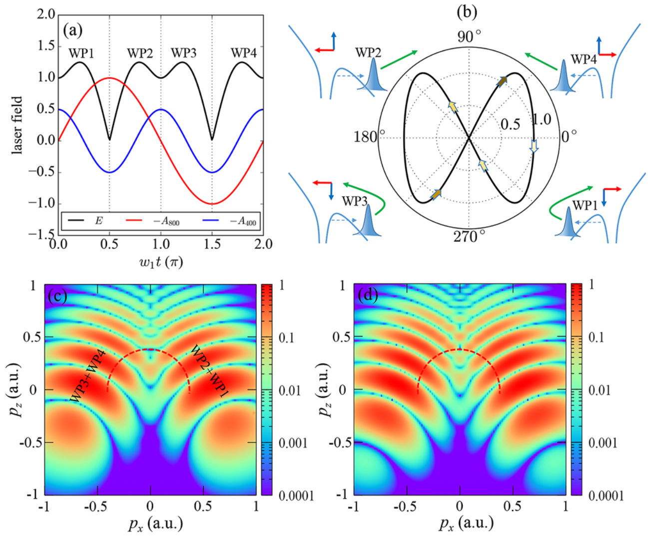

FIG. 3. (a) The temporal sketch of the OTC field for $\Delta\varphi = 0.5\pi$ with respect to one 800 nm cycle. The black line, red line, and blue line in (a) indicate the synthesized light electric field, negative vector potentials of 800 nm light and that of 400 nm light, respectively. (b) The spatial view of the OTC field and the emitting wave packets in the polarization plane (horizontal direction is the x axis and vertical direction is the z axis). In (b) the black line depicts the track of the end point of the synthesized electric-field vector in one 800 nm cycle (the radial coordinate represents the electric-field strength and the angular coordinate means its direction), and the yellow arrows on the black line mark the increase of time as the color gradually deepens. The four outer subplots in (b) depict the components of laser electric fields (the red arrow displays the 800 nm light and the blue solid arrow shows the 400 nm light) when the corresponding wave packet tunnels, and describe the wave-packet subsequent motions with green arrows schematically. (c) The subcycle interferogram calculated by the SFA model employing the saddle-point method without the plain sub-barrier phase. (d) The same calculation as (c) but with the plain sub-barrier phase.

We further calculate their interferograms by the SFA model employing the saddle-point method. This can remove the effect of Coulomb scattering and intercycle interference structures. The subcycle interferograms with and without sub-barrier phase are shown in Figs. 3(c) and 3(d), respectively. The interference fringes are sensitive to the plain sub-barrier phase $\mathrm{Re}[S_0(\boldsymbol{p}, t_s, t_r)]$. When the calculation includes the sub-barrier phase, the number of the fringes in the left or right momentum plane increases from 8 to 10. We also mark the first ATI ring with a red dashed curve in the interferograms. The sub-barrier phase indeed leaves the fingerprint on the number of the intersections between these fringes and the ATI ring, leading to an increase of two more maxima along the curve.

At this phase delay we take the interference between WP3 and WP4 as an example to explain the spatial dependence of the sub-barrier phase in OTC fields. The dominant sub-barrier phase $\mathrm{Re}[S_0(\boldsymbol{p}, t_s^{(i)}, t_r^{(i)})]$ can be evaluated analytically as

$$\begin{aligned}\mathrm{Re}[S_0(\boldsymbol{p}, t_s^{(i)}, t_r^{(i)})] &= -\frac{p_x E_{800}}{\omega_1^2}\cos(\omega_1 t_r^{(i)})[1-\cosh(\omega_1 t_i^{(i)})] \\ &+ \frac{E_{800}^2}{8\omega_1^3}\sin 2(\omega_1 t_r^{(i)})[1-\cosh(2\omega_1 t_i^{(i)})] \\ &- \frac{p_z E_{400}}{\omega_2^2}\cos(\omega_2 t_r^{(i)}+\Delta\varphi)[1-\cosh(\omega_2 t_i^{(i)})] \\ &+ \frac{E_{400}^2}{8\omega_2^3}\sin 2(\omega_2 t_r^{(i)}+\Delta\varphi)[1-\cosh(2\omega_2 t_i^{(i)})]. \qquad (2)\end{aligned}$$

From Eq. (2), one can find that the sub-barrier phase contains the two-dimensional tunneling geometry, which is closely related with the synthesized electric field. As shown in Fig. 3(b), for those two wave packets, the ionizing electric fields are with the equal value but in opposite directions. We show the distributions of the probability and initial phase of WP3 and WP4 in the final momentum plane in Fig. 4 at $\Delta\varphi = 0.5\pi$. Those two interfered WPs are driven to be totally overlapped in the final momentum plane as seen in Figs. 4(a) and 4(b). In Figs. 4(c) and 4(d), the direction of the phase gradient is approximately along the synthesized electric field, and their phase distributions are opposite. Therefore, the effect of the initial phase is significantly enhanced at this delay.

The signature of the sub-barrier phase can also be found at other phase delays. For example, at $\Delta\varphi = 0.25\pi$, the electron momentum distributions calculated by the CCSFA model with and without the sub-barrier phase are shown in Fig. 5. At this delay, the WP3 and WP4 have different ionization probabilities, and they are partially overlapped in

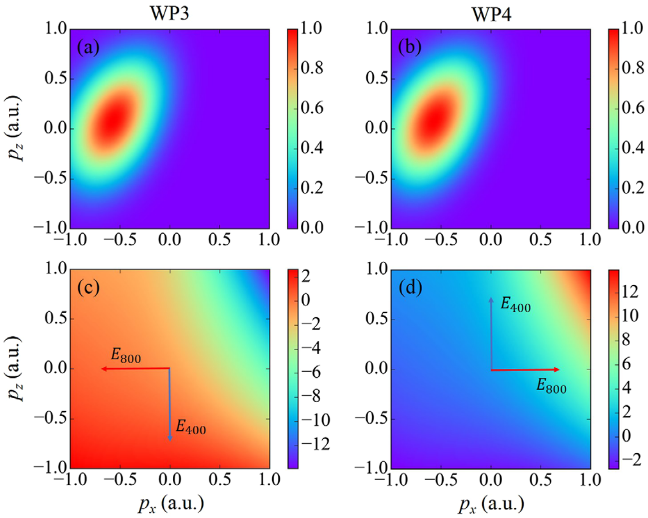

FIG. 4. The distribution of probability [(a) and (b)] and plain sub-barrier phase [(c) and (d)] of WP3 (left column) and WP4 (right column) in the final momentum plane. The ionization probability is normalized to the maximum, and the phase value is the real value in radian units.

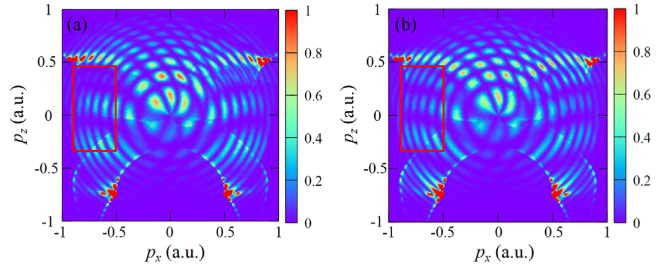

FIG. 5. Electron momentum distributions in the OTC field at $\Delta\varphi = 0.25\pi$ calculated by the CCSFA model without the sub-barrier phase (a) and with the sub-barrier phase (b). The interference pattern between WP3 and WP4 is marked within the red rectangles.

the final momentum plane because of the asymmetry of the light field [29]. On the other hand, the signs of their sub-barrier phases are not opposite [29]. The interference pattern between those WPs is not well separated, and it is mainly distributed within the red rectangles in Fig. 5. Again, CCSFA simulation with sub-barrier phase agrees better with the experiment.

One noted that, at $\Delta\varphi = 0.75\pi$, although the synthesized vector potential is the same as that of $\Delta\varphi = 0.25\pi$, the probability and phase for WP3 and WP4 are very different [29]. The scattering behavior of those packets is essentially different for those two delays, and thus their momentum distributions are completely different [24]. At the phase delay of $\Delta\varphi = 0$, the WP3 and WP4 are much less spatially overlapped [29]. Thus, it is hard to observe the interference signature between them. The subcycle interference between W2 and WP4 comes into the dominant role.

The sub-barrier phase should be inevitably involved for photoelectron interference or holography in the tunneling-related processes [30–33]. Usually, it is hard to observe from electron momentum distributions in a linear laser field because of hard rescattering and the Coulomb focusing effect. Using the OTC fields with comparable intensities, one can reveal the sub-barrier phase of strong-field tunneling ionization from the spatially separated subcycle interference pattern.

In summary, we have measured the electron momentum distributions of Argon atoms in comparable-intensity OTC fields. Based on this interaction geometry, we demonstrate a spatiotemporal interferometer and show that the sub-barrier phase of strong-field tunneling ionization can be recorded on the interferograms. Since the sub-barrier phase originates from the tunneling, it definitely imprints its effect on the coherent processes in tunneling-related phenomena. Note that the electron momentum distribution calculated by the CCSFA model agrees better with the experiment. As known, the nonadiabatic effect is naturally included in the CCSFA model, and thus the theoretically predicted non-adiabatic effect by OTC fields [19] is verified by this measurement when comparing with the adiabatic model [34]. The spatiotemporal interferometer could also be potentially used to probe the photoelectron phase of aligned molecules in strong-field ionization [35].

This work is supported by the National Science Foundation of China (Grants No. 11434002 and No. 11527901).

---

[*] Yunquan.liu@pku.edu.cn

[1] P. B. Corkum, Phys. Today **64**, No. 3, 36 (2011).
[2] M. Li, Y. Liu, H. Liu, Q. Ning, L. Fu, J. Liu, Y. Deng, C. Wu, L. Peng, and Q. Gong, Phys. Rev. Lett. **111**, 023006 (2013).
[3] X. B. Bian, Y. Huismans, O. Smirnova, K. J. Yuan, M. J. J. Vrakking, and A. D. Bandrauk, Phys. Rev. A **84**, 043420 (2011).
[4] M.-M Liu, M. Li, C. Wu, Q. Gong, A. Staudte, and Y. Liu, Phys. Rev. Lett. **116**, 163004 (2016).
[5] M. Spanner, O. Smirnova, P. B. Corkum, and M. Y. Ivanov, J. Phys. B **37**, L243 (2004).
[6] S. Popruzhenko and D. Bauer, J. Mod. Opt. **55**, 2573 (2008).
[7] T.-M. Yan, S. V. Popruzhenko, M. J. J. Vrakking, and D. Bauer, Phys. Rev. Lett. **105**, 253002 (2010).
[8] L. Torlina, J. Kaushal, and O. Smirnova, Phys. Rev. A **88**, 053403 (2013).
[9] T.-M. Yan and D. Bauer, Phys. Rev. A **86**, 053403 (2012).
[10] F. Lindner, M. G. Schatzel, H. Walther, A. Baltuska, E. Goulielmakis, F. Krausz, D. B. Milosevic, D. Bauer, W. Becker, and G. G. Paulus, Phys. Rev. Lett. **95**, 040401 (2005).
[11] O. Pedatzur *et al.* Nat. Phys. **11**, 815 (2015).
[12] M. Kitzler and M. Lezius, Phys. Rev. Lett. **95**, 253001 (2005).
[13] I. J. Kim, C. M. Kim, H. T. Kim, G. H. Lee, Y. S. Lee, J. Y. Park, D. J. Cho, and C. H. Nam, Phys. Rev. Lett. **94**, 243901 (2005).
[14] H. Niikura, H. J. Wörner, D. M. Villeneuve, and P. B. Corkum, Phys. Rev. Lett. **107**, 093004 (2011).
[15] G. Laurent, W. Cao, H. Li, Z. Wang, I. Ben-Itzhak, and C. L. Cocke, Phys. Rev. Lett. **109**, 083001 (2012).
[16] X. Gong, P. He, Q. Song, Q. Ji, H. Pan, J. Ding, F. He, H. Zeng, and J. Wu, Phys. Rev. Lett. **113**, 203001 (2014).
[17] M. Li, J. W. Geng, M. M. Liu, X. Zheng, L. Y. Peng, Q. Gong, and Y. Liu, Phys. Rev. A **92**, 013416 (2015).
[18] M. Richter, M. Kunitski, M. Schöffler, T. Jahnke, L. P. H. Schmidt, M. Li, Y. Liu, and R. Dörner, Phys. Rev. Lett. **114**, 143001 (2015).
[19] J.-W. Geng, W.-H. Xiong, X.-R. Xiao, L.-Y. Peng, and Q. Gong, Phys. Rev. Lett. **115**, 193001 (2015).
[20] L. V. Keldysh, Sov. Phys. JETP **20**, 1307 (1965).
[21] F. H. M. Faisal, J. Phys. B **6**, L89 (1973).
[22] H. R. Reiss, Phys. Rev. A **22**, 1786 (1980).
[23] J. Ullrich, R. Moshammer, A. Dorn, R. Dörner, L. Ph. H. Schmidt, and H. Schmidt-Böcking, Rep. Prog. Phys. **66**, 1463 (2003).
[24] L. Zhang, X. Xie, S. Roither, D. Kartashov, Y. L. Wang, C. L. Wang, M. Schöffler, D. Shafir, P. B. Corkum, A. Baltuška, I. Ivanov, A. Kheifets, X. J. Liu, A. Staudte, and M. Kitzler, Phys. Rev. A **90**, 061401(R) (2014).

[25] S. G. Yu, Y. L. Wang, X. Y. Lai, Y. Y. Huang, W. Quan, and X. J. Liu, Phys. Rev. A **94**, 033418 (2016).

[26] D. B. Milošević, G. G. Paulus, D. Bauer, and W. Becker, J. Phys. B **39**, R203 (2006).

[27] A. M. Perelomov and V. S. Popov, Sov. Phys. JETP **25**, 336 (1967). The Coulomb singularity is regularized through matching to the field-free initial-state wave function.

[28] V. Mosert and D. Bauer, Comput. Phys. Commun. **207**, 452 (2016).

[29] See Supplemental Material at http://link.aps.org/supplemental/10.1103/PhysRevLett.119.073201 for the interference dynamics of WP3 and WP4 at different phase delays.

[30] Y. Huismans *et al.*, Science **331**, 61 (2011).

[31] Ph. A. Korneev, S. V. Popruzhenko, S. P. Goreslavski, T.-M. Yan, D. Bauer, W. Becker, M. Kübel, M. F. Kling, C. Rödel, M. Wünsche, and G. G. Paulus, Phys. Rev. Lett. **108**, 223601 (2012).

[32] X. Xie, S. Roither, D. Kartashov, E. Persson, D. G. Arbó, L. Zhang, S. Gräfe, M. S. Schöffler, J. Burgdörfer, A. Baltuška, and M. Kitzler, Phys. Rev. Lett. **108**, 193004 (2012).

[33] M. Haertelt, X.-B. Bian, M. Spanner, A. Staudte, and P. B. Corkum, Phys. Rev. Lett. **116**, 133001 (2016).

[34] M. Li, J.-W. Geng, H. Liu, Y. Deng, C. Wu, L.-Y. Peng, Q. Gong, and Y. Liu, Phys. Rev. Lett. **112**, 113002 (2014).

[35] M. Meckel, A. Staudte, S. Patchkovskii, D. M. Villeneuve, P. B. Corkum, R. Dörner, and M. Spanner, Nat. Phys. **10**, 594 (2014).